J Mater Sci (2007) 42:5700–5713
DOI 10.1007/s10853-006-0704-5

Identification of microstructural zones and thermal cycles in a weldment of modified 9Cr-1Mo steel

V. Thomas Paul · S. Saroja · P. Hariharan · A. Rajadurai · M. Vijayalakshmi

Received: 22 March 2006 / Accepted: 24 July 2006 / Published online: 3 April 2007

Abstract This paper presents the results of a study on the microstructural and microchemical variations in a multi-pass Gas Tungsten Arc weld (GTAW) of modified 9Cr-1Mo steel. The changes brought about in the steel due to the heating and cooling cycles during welding and the subsequent effects due to reheating effects during multi-pass welding are described. Detailed analytical transmission electron microscopy has been carried to study the type and composition of the primary and secondary phases in this steel. The systematic changes in microstructural parameters such as Prior Austenite Grain Size, martensite lath size, number density, size and microchemistry of carbides, have been understood based on the different transformations that the steel undergoes during the heating and cooling process. Based on the observed microstructure, an attempt has been made to identify distinct microstructural zones and possible thermal cycles experienced by different regions of the weldment.

V. T. Paul · S. Saroja (✉) · M. Vijayalakshmi
Physical Metallurgy Section, Metallurgy and Materials Group,
Indira Gandhi Centre for Atomic Research,
Kalpakkam 603 102, India
e-mail: saroja@igcar.gov.in

P. Hariharan
Department of Manufacturing Engineering,
Anna University, Chennai 600 025, India

A. Rajadurai
Department of Production Engineering,
Madras Institute of Technology,
Chennai 600 044, India

Introduction

Modified 9Cr-1Mo steel (grade P91 & T91) finds application in power plants for the construction of steam generators, due to its excellent high temperature creep strength and high resistance to stress corrosion cracking [1–5]. Earlier investigations of this steel indicate that P91 can be used safely up to a temperature of 923 K [4]. In addition to higher creep strength, grade 91 steel has good ductility and toughness, low thermal expansion coefficient, good hardenability, resistance towards hydrogen embrittlement and no susceptibility to reheat cracking. Basically, P91 has a martensitic structure, which remains unchanged even for a low cooling rate from austenite. A low concentration of carbon is preferred to achieve a high M_s (~400 K) as well as a low hardness of the martensite. Furthermore, the steel is made superior to conventional 9Cr-1Mo steel with respect to creep properties by the controlled addition of V and Nb [1]. Relatively stable $M_{23}C_6$ carbides, which precipitate on boundaries during tempering, provide basic creep strength to the steel by retarding the subgrain growth [6]. Finely dispersed, highly stable intergranular V (Nb) carbides/nitrides (MX) formed during tempering provide an additional source of creep strength [7–9]. Very fine mono-carbides V (Nb) C that precipitate within the subgrains pin down mobile dislocations and also increase the creep strength significantly.

Although this steel offers good weldability, the mechanical properties of the welded joints are found to be inferior compared to the base metal [10, 11]. The microstructures that form in the Heat Affected Zone (HAZ) are highly heterogeneous due to the different heating/cooling rates experienced at various distances from the fusion line. The zone is classified as Coarse Grained (CGHAZ), Fine Grained (FGHAZ) and Intercritical (ICHAZ) Heat

Affected Zones, based on their characteristic microstructures. Failure of the weld joint occurs in the fine grained/intercritical heat affected zone during high temperature service, which is often referred as the Type IV cracking [11–13]. Studies on simulated HAZ microstructures have shown that tensile/creep properties of the FGHAZ/ICHAZ are considerably lower, whereas that of the coarse grained HAZ is better than the weld or base metal [14–16]. Therefore, the microstructural and microchemical changes that take place in the HAZ during welding need to be well understood as they influence the performance of the weld joints during service. Hence, a detailed study was performed to characterize the different microstructures introduced during welding as a function of the thermal cycles experienced by each region of the weldment.

Experimental

The modified 9Cr-1Mo steel was supplied by M/s Midhani, India, as round forgings in the normalized (1,333K—1h) and tempered (1,033 K—1h) condition. The chemical composition of the steel is given in Table 1. 10-mm thick plates machined out of the bar were used for fabrication of the weld. Welding was performed by the manual GTAW process using modified 9Cr-1Mo filler wire, supplied by M/s Metrode, United Kingdom. The filler wire composition and welding parameters are given Tables 2 and 3, respectively. The schematic weld geometry is shown in Fig. 1. A weld height of approximately 6 mm was achieved by five successive layers. The number of passes was 12 in each layer. The weldment is classified as regions W1, W2 and W3 within the weld and HAZ1, HAZ2 and unaffected BM in the base metal, as shown in the Figure for the purpose of this study.

The specimens from sections taken perpendicular to weld interface were prepared metallographically by standard preparation procedures. Optical microscopy and microhardness measurements were performed using a Leica MeF4A microscope and Leitz Miniload II Vickers Hardness Testing machine under an applied load of 100 g. The microstructure was studied by Scanning Electron Microscopy using a Philips XL 30 ESEM, with Energy Dispersive Spectroscopy. Analytical Transmission Electron Microscopy (ATEM) was performed on thin foils to study the structure and on extraction replicas to identify the type and chemistry of secondary phases. Thin-foil specimens for transmission electron microscopy were prepared by the window thinning method using 10% perchloric acid in methanol as the electrolyte. Extraction replicas were prepared from well polished & carbon coated specimens using Vilella's reagent. ATEM was carried out using a Philips CM 200 microscope equipped with a super ultra-thin window (SUTW) energy dispersive X-ray spectrometer (EDS) at an operating voltage of 120–160 kV. Quantification of EDS spectra was done using the Cliff Lorimer method with K_{AB} values generated from standard samples of known chemical composition.

Table 1 Chemical composition of Base metal (wt.%)

Cr	Mo	Ni	C	Mn	Si
8.72	0.90	0.10	0.096	0.46	0.32
S	P	V	Nb	N	Fe
0.006	0.012	0.22	0.08	0.051	Bal.

Table 2 Filler wire composition (wt.%)

Cr	Mo	Ni	C	Mn	Si	S
8.72	0.95	0.80	0.1	0.51	0.25	0.003
P	V	Nb	N	Cu	O	Fe
0.004	0.19	0.07	0.04	0.01	0.004	Bal.

Results and discussion

The results of this study are classified under two major themes, namely: (1) Microstructural heterogeneity across the weldment (Weld, HAZ1, HAZ2, and Base metal) during solidification, and (2) Effect of reheating on the microstructure of the weld. The results are presented in the following sequence. Section 'Characterization of the base metal' deals with the characterization of base metal and Section 'Microstructural characterization of weld zone' describe the weld microstructure. Microstructural heterogeneity in HAZ is discussed in Section 'Microstructural modifications in the Heat Affected Zone'. Sections 'Effect of reheating on the microstructure of weld zone' and

Table 3 Welding procedure and parameters

Process	Manual GTAW
Voltage	12 V
Current	90 amps
Filler wire ϕ	2 mm
Welding speed	70 mm/min
No. of layers	5
No. of passes per layer	12
Overlap between passes	~2 mm
Size of the weld bead	~6 mm (W) × 1.2 mm(H)
Pre-heat	200 °C
Interpass temperature	200 °C
Shielding gas	Argon @ 10 L/min

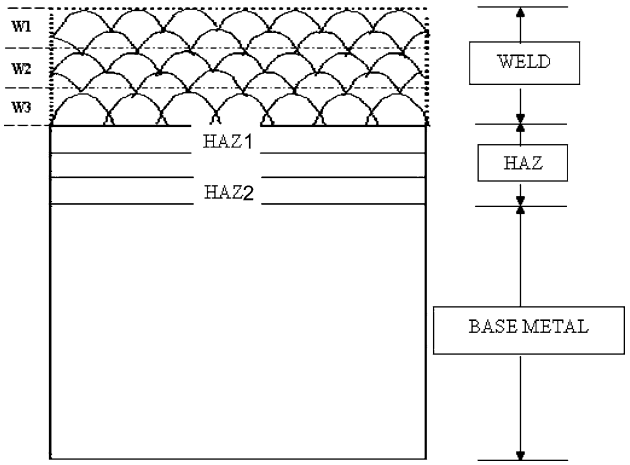

Fig. 1 Geometry of the weld (Schematic)

'Thermal cycles of different regions of weldment' describe the effect of reheating in the weld zone and thermal cycles experienced at different regions of weld, respectively.

Characterization of the base metal

The microstructure of the base metal in the normalized and tempered condition is shown in Fig. 2a. A tempered martensitic microstructure with abundant precipitates along the prior austenite and martensitic lath boundaries is observed. The average austenite grain size was about 40 μm with an average hardness level of 200VHN. The thin foil TEM micrograph in Fig. 2b reveals the finer features showing well-defined, individual laths of tempered martensite with coarse globular carbides along the boundaries. The average lath size was measured to be in the range of 0.5–1 μm. It was difficult to observe the finer carbides due to the high density of dislocations [17], uniformly distributed in the martensitic matrix. Hence, further analysis to identify the type, amount and microchemistry of carbides was carried out using extraction replicas. Figure 2c shows a TEM micrograph of the carbon extraction replica of the base metal. The presence of coarse boundary and interlath precipitates of both globular and lenticular morphologies (marked A) was observed. The sizes ranged from 0.2 μm to 0.4 μm. Apart from these, a uniform distribution of fine (100–150 nm) and extremely fine (40–80 nm) carbides (marked B in Fig. 2c) was observed within the laths. A typical selected area electron diffraction (SAD) pattern from a globular carbide of type A is shown in Fig. 2d along with its key in Fig. 2e. The analysis of SAD pattern confirms that the carbide is M_{23} C_6 along the $\langle \bar{1}\ 1\ 1 \rangle$ zone axis. The microdiffraction carried out on fine carbides uniformly present within the laths also identified them as $M_{23}C_6$.

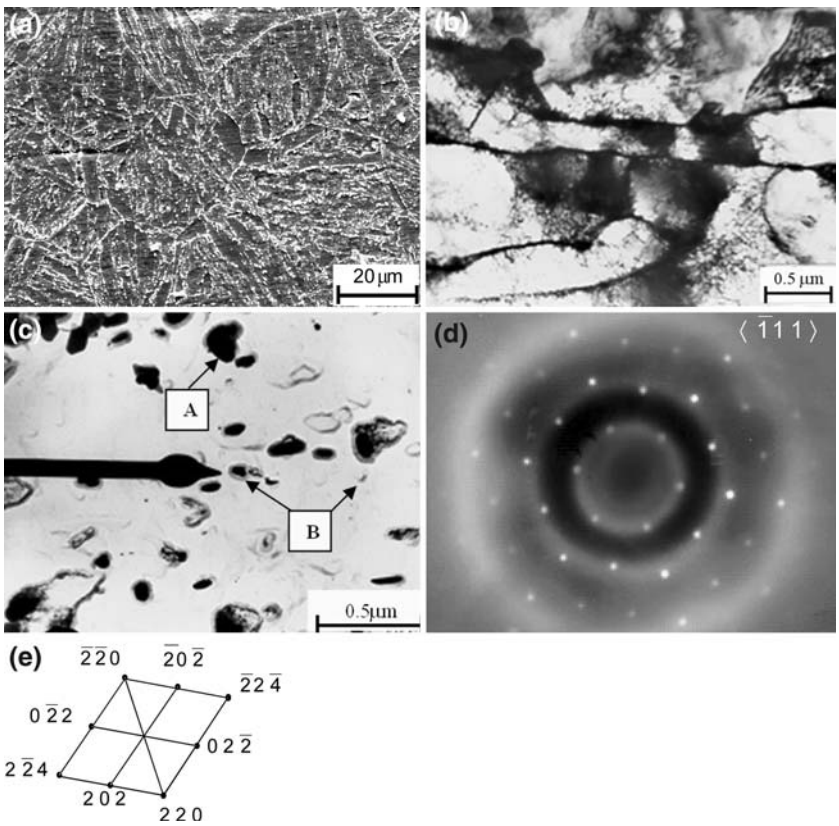

Fig. 2 Microstructural details of base metal (**a**) SEM micrograph showing prior austenite grain boundaries and complete martensitic substructure (**b**) Retention of martensitic laths with grain boundary carbides (**c**) presence of coarse $M_{23}C_6$ and fine MX precipitates (**d**) Diffraction pattern from $M_{23}C_6$ carbide (marked A in **c**) taken along $\langle \bar{1}\ 1\ 1 \rangle$ zone axis, and (**e**) key to the above pattern

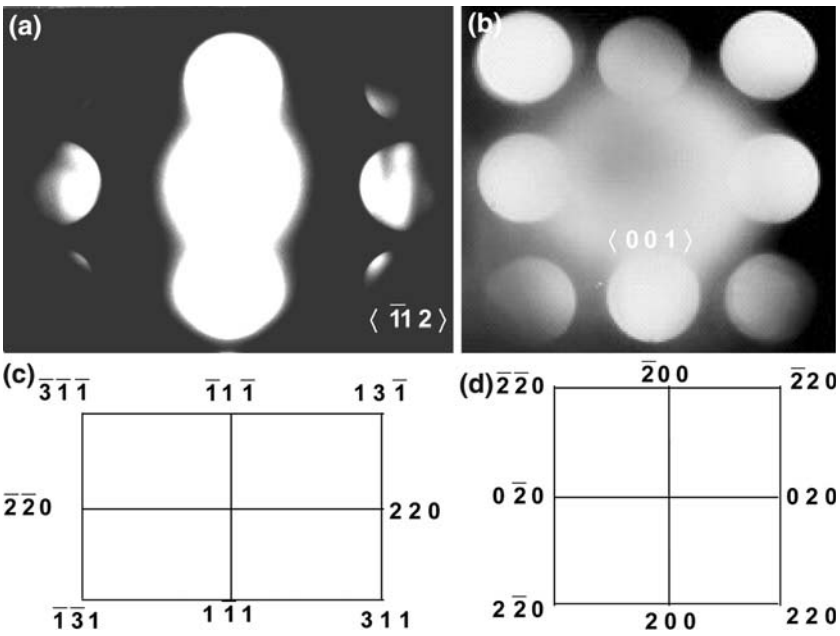

Fig. 3 Microdiffraction patterns from fine intralath carbides (MX) marked B in Fig. 2(b) taken (**a**) along ⟨1̄ 1 2⟩ zone axis (**b**) along ⟨0 0 1⟩ zone axis and (**c** & **d**) key to diffraction pattern in (**a**) & (**b**), respectively

Generally, the presence of fine MX type of carbides augments the creep strength of the modified steels in the normalized and tempered condition [3, 9, 18, 19]. Figure 3a and b shows the diffraction pattern obtained from these fine carbides (marked B) along with the keys (Fig. 3c and d). Analysis of the diffraction pattern showed that these are MX-type of carbides along ⟨1̄ 1 2⟩ and ⟨0 1 1⟩ zone axes. There was no evidence for the formation of M_2X type of precipitate, which is most commonly found in plain 9Cr-1Mo steels. It is possible that during the tempering of 1 h at 1,033 K, even if M_2X were to form, the time was quite sufficient for its conversion to $M_{23}C_6$. This observation is in agreement with literature [7, 18], where it is reported that M_2X carbides that formed at 1,033 K during the early stages of tempering were replaced by M_{23} C_6 and MX precipitates within an hour of tempering.

The microchemistry of different types of carbides was studied using Energy Dispersive X-ray Spectroscopy (EDS). Figure 4a shows an EDS spectrum obtained from a typical $M_{23}C_6$-type carbide. It is Cr-rich, although it

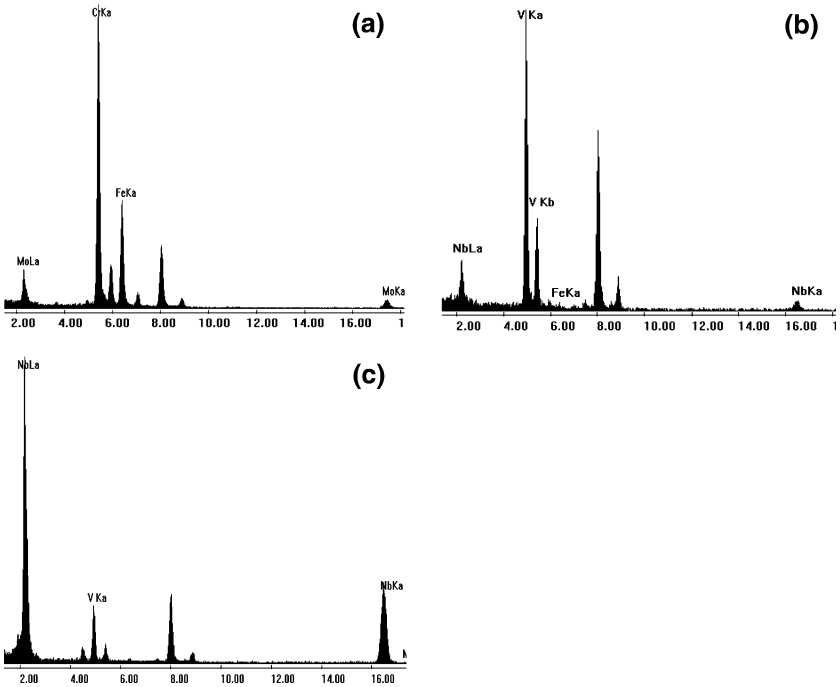

Fig. 4 EDS spectra obtained from various types of carbides present in the base metal showing (**a**) Cr-rich $M_{23}C_6$ (**b**) V-rich MX and (**c**) Nb-rich MX

contains a large amount of iron and molybdenum. The average Cr/Fe ratio was found to be 2.5. The EDS spectra from MX carbides are shown in Fig. 4b and c. Although majority of the precipitates were rich in vanadium, a few very fine niobium-rich precipitates were also observed. Most of these carbides were either V- or Nb- rich with small solubility for the other element. The abundance of vanadium-rich precipitates can be understood from the steel composition. Although the identity of X could not be established unequivocally during this study, it is expected to be a carbonitride. Therefore, the microstructure of the base metal can be summarized as tempered lath martensite with copious precipitation of Cr-rich $M_{23}C_6$ and a fine distribution of monocarbides of V and Nb (V(Nb)X).

Microstructural characterization of weld zone

Macroscopic examination of the weld region shows the thickness of weld to be around 6 mm since it was prepared by deposition of multiple passes and multiple layers of weld metal on the plate, as shown in Fig. 1. This zone can be further subdivided into region W1, W2 and W3. W1 refers to regions that have solidified from the liquid metal and not undergone any further reheating, W2 and W3, refer to regions that have been reheated after solidification due to multiple layers. Further discussion on weld zone is therefore confined to region W1 alone.

Figure 5a shows the optical micrograph of the weld zone. A columnar structure typical of directional solidification is observed since this region has formed by solidification of the liquid metal. The region had a uniform hardness of about 420 VHN, which is in agreement with the observed microstructure of martensite. The SEM micrograph in Fig. 5b shows elongated prior austenite grains with an average width of 10 μm and length of 40 μm. A fully martensitic structure was observed with no evidence of delta ferrite (δ-ferrite) or pro-eutectoid ferrite (α-ferrite). This is consistent with the high microhardness (420 VHN). This observation also suggests that the cooling rate in the temperature regimes for the two transformations ($L \rightarrow \gamma$ & $\gamma \rightarrow \alpha'$) has been fast enough to suppress the nucleation of δ and α ferrite. The thin-foil micrograph of the top region of the weld in Fig. 5c shows lath martensite. A high dislocation density was observed within the laths with no evidence of carbides. The lath size was found to be uniform, in the range of 0.4–0.5 μm. The carbon extraction replica examination also confirmed the absence of carbides.

Based on the pseudo binary Fe–Cr phase diagram for 0.1% C [2], the weld region is expected to undergo the following transformations.

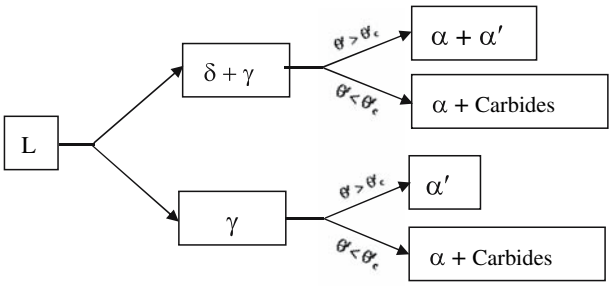

The chromium equivalent of the steel is given by the following expression [20].

$$\begin{aligned} Cr_{eq} = &\%Cr + 6(\%Si) + 4(\%Mo) + 1.5(\%W) + 11(\%V) \\ &+ 5(\%Nb) + 12(\%Al) + 8(\%Ti) - 40(\%C) \\ &- 2(\%Mn) - 4(\%Ni) - 2(\%Co) - 30(\%N) - \%Cu \end{aligned}$$

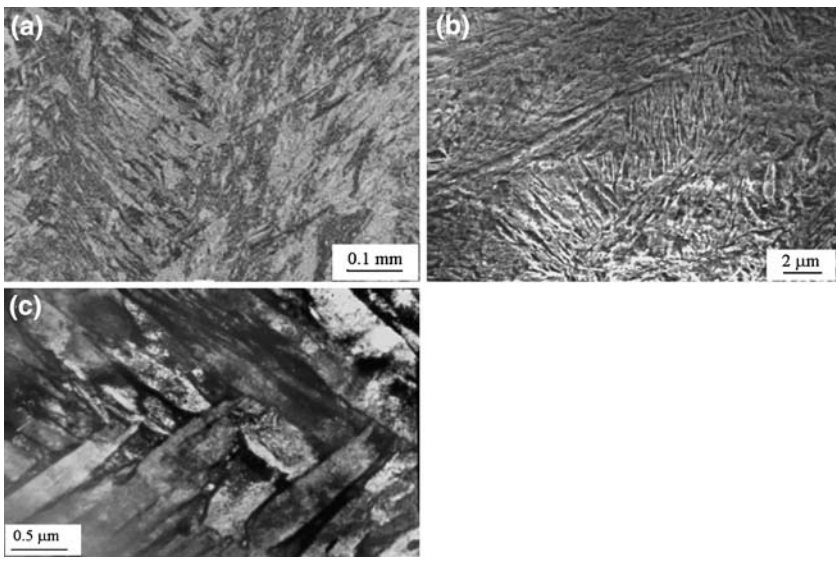

Fig. 5 Microstructure of weld zone (**a**) Optical micrograph showing the typical columnar cast structure (**b**) SEM micrograph showing the completely martensitic structure with elongated prior austenite grains, and (**c**) TEM micrograph showing martensitic laths with a high dislocation density

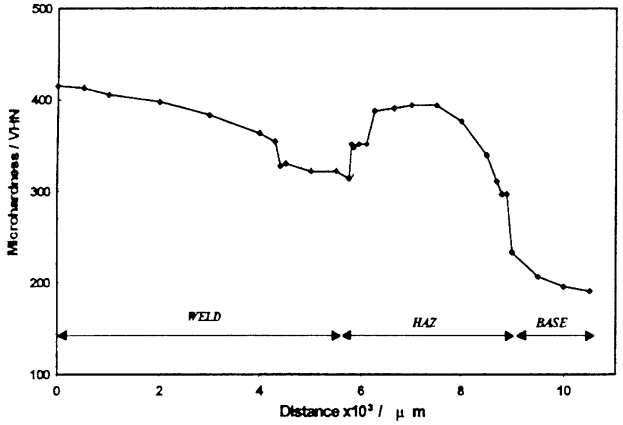

Fig. 6 Microhardness profile across the weldment consisting of weld, HAZ and base metal showing a continuous decrease in hardness from weld top to the weld metal fusion line, and higher hardness at coarse grained HAZ compared to fine grained HAZ

The chromium equivalent estimated for the electrode composition is about 7.03. The absence of δ or α ferrite is consistent with the low value of chromium equivalent and the high cooling rate in the weld. Retention of delta ferrite is reported in this steel for a chromium equivalent ≥9wt.% [21, 22]. The transformations in the weld metal, which has undergone solidification but no reheating, can therefore be summarized as follows:

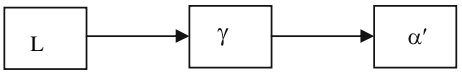

The minor microstructural variations observed across the thickness of the weld due to secondary processes during reheating would be discussed later.

Microstructural modifications in the Heat Affected Zone

The Heat Affected Zone (HAZ) is the most important region in a weldment especially for ferritic alloys since most of the industrial failures occur in this region, more precisely at inter critical region [11, 23–25]. The microstructural variations in the HAZ are also reflected in the microhardness profile of the cross section. The microhardness profile using a load of 100 g taken across the weldment consisting of weld, HAZ, and base metal is shown in Fig. 6. The micrographs of the regions consisting of fusion zone and HAZ are shown in Fig. 7a–c. The observations made from Figs. 6 and 7 are as follows:

(i) The width of the HAZ is about 3 mm, which is in agreement with the observed microhardness profile.
(ii) A continuous reduction in the prior austenite grain size was observed in HAZ, resulting in a coarse-grained region (Fig. 7b) adjacent to weld and a

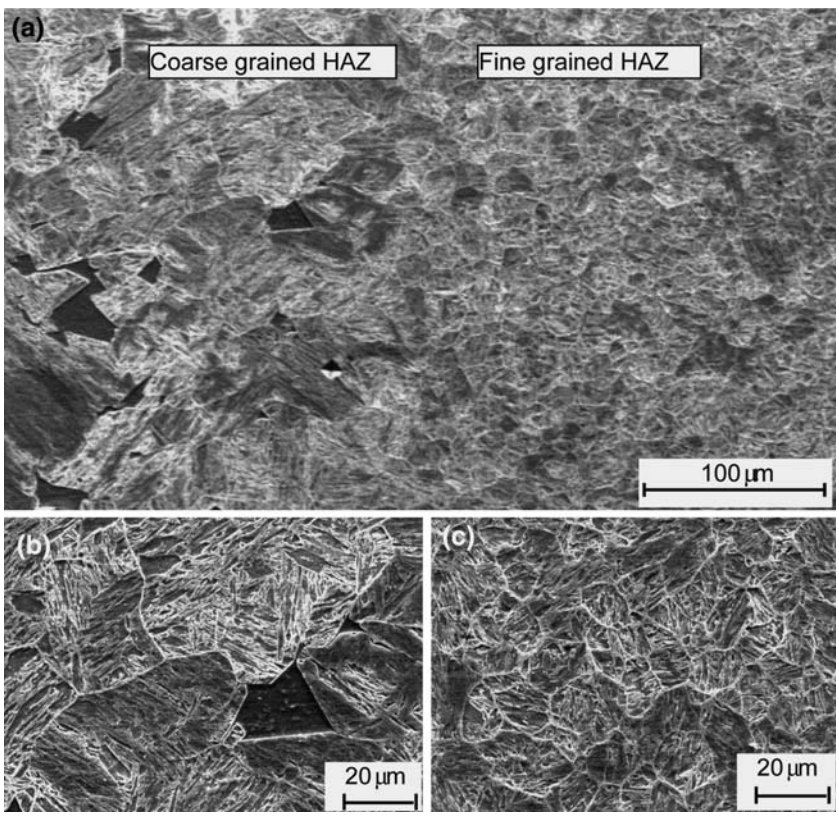

Fig. 7 SEM micrographs showing (**a**) various microscopic regions of Heat Affected Zone (**b**) Coarse grained HAZ region with evidence for presence of delta ferrite, and (**c**) Fine grained HAZ

fine-grained region (Fig. 7c) adjacent to unaffected base metal.

(iii) A decrease in hardness from 350 to 200 VHN was observed in regions that included HAZ and extended into the base metal; an increase in hardness between fusion zone and fine-grained region was followed by a continuous reduction to base metal values.

(iv) Stringers of another phase, possibly δ-ferrite, were observed along the weld-base metal interface.

It was noted that there were microstructural variations within the HAZ, which has been studied in detail at typically two different depths, termed as HAZ1 and HAZ2.

Microstructure of HAZ1

This region, which is closer to the fusion zone, exhibited a hardness of 350–400 VHN as compared to 200 VHN for the base metal. The SEM micrograph of this region in Fig. 7b shows prior austenite grains, with sizes ranging from 50 μm to 70 μm, and a fully martensitic structure. Few stringers free from laths are observed adjacent to the weld fusion line. Microhardness measurements using lower loads showed lower hardness values in the range of 200–240 VHN, compared to 400 VHN for the martensite, which suggested that these stringers were the delta ferrite phase. The formation of delta ferrite in the fusion zone can be understood in terms of the low cooling rate at the interface as compared to the weld region. The higher Cr_{eq} of the base metal (10.38) as compared to weld metal (7.03) would also aid the formation of delta ferrite during cooling. The presence of delta ferrite in the HAZ region close to fusion boundary was also observed in this steel during laboratory simulated heat treatments, and is also supported by literature [26–29].

The thin-foil TEM micrograph (Fig. 8a) shows the presence of a parallel array of martensite laths. The average size was measured as 0.35 μm as compared to 0.7 μm in the base metal. The TEM micrograph of the carbon extraction replica (Fig. 8b) obtained from this region shows a reduction in the number density as well as size of carbides as compared to the base metal, especially the lath boundary carbides. The average carbide size is about 0.1 μm as compared to 0.2–0.3 μm for carbides in the base metal. A Selected Area Diffraction (SAD) pattern from a coarse carbide, given as an inset in Fig. 8b, shows an $M_{23}C_6$ carbide along $\langle \bar{1}\ 1\ 1 \rangle$ zone axis. EDS analysis from a large number of $M_{23}C$type carbides showed that they are all rich in Cr. Most of the $M_{6\ 23}C_6$ carbides had a Cr/Fe ratio similar to that obtained from the base metal. However, a few carbides with a lower (<1.5) Cr/Fe were also detected. Analysis of the carbides in this region also revealed the rare presence of NbX (Fig. 8d), although no evidence for VX could be obtained. The presence of NbX can be understood in terms of the stability of this carbide, which has also been reported by other workers [7, 18]. The absence of VX is probably due to high temperatures experienced by this region and its fine initial size. It is expected that the $M_{23}C_6$ precipitates with Cr/Fe ratio similar to those in base metal are pre-existing carbides present in the normalized and tempered steel. This is due to the brief time of the region at high temperature, during which the complete

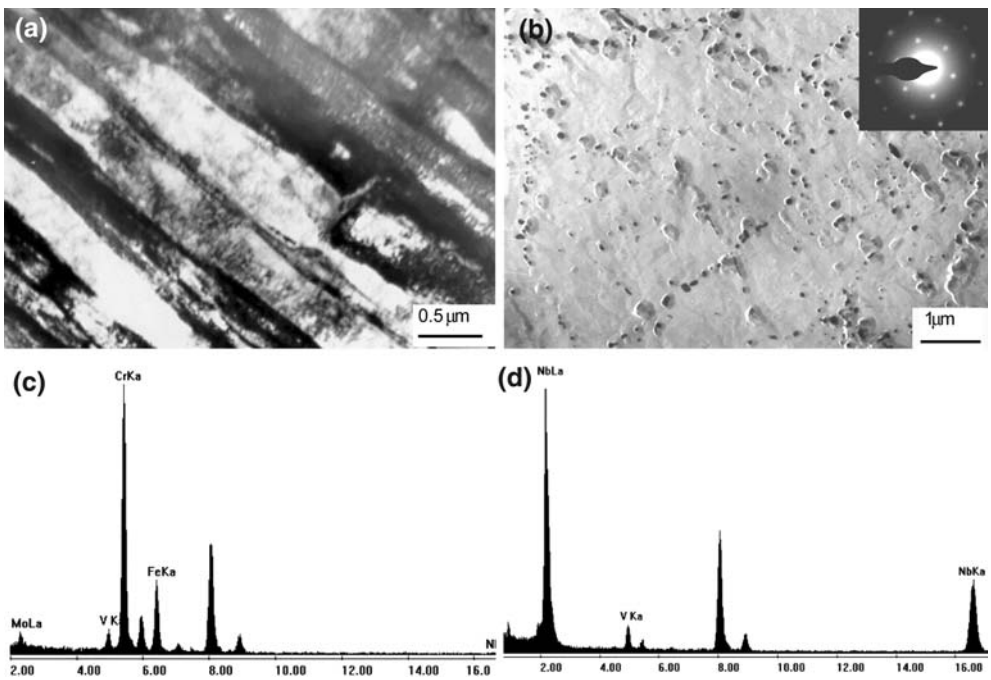

Fig. 8 Microstructural characterization and distribution of secondary phases in HAZ1 (**a**) TEM micrograph showing a fine lath martensitic structure (**b**) Evidence for fine carbides compared to base metal; Inset shows SAD pattern from a coarse carbide along $\langle \bar{1}\ 1\ 1 \rangle$ zone axis (**c**) EDS spectrum from a $M_{23}C_6$ carbide with higher Cr/Fe ratio illustrating retention of carbides present in the N&T steel, and (**d**) EDS spectrum from NbX which remain undissolved

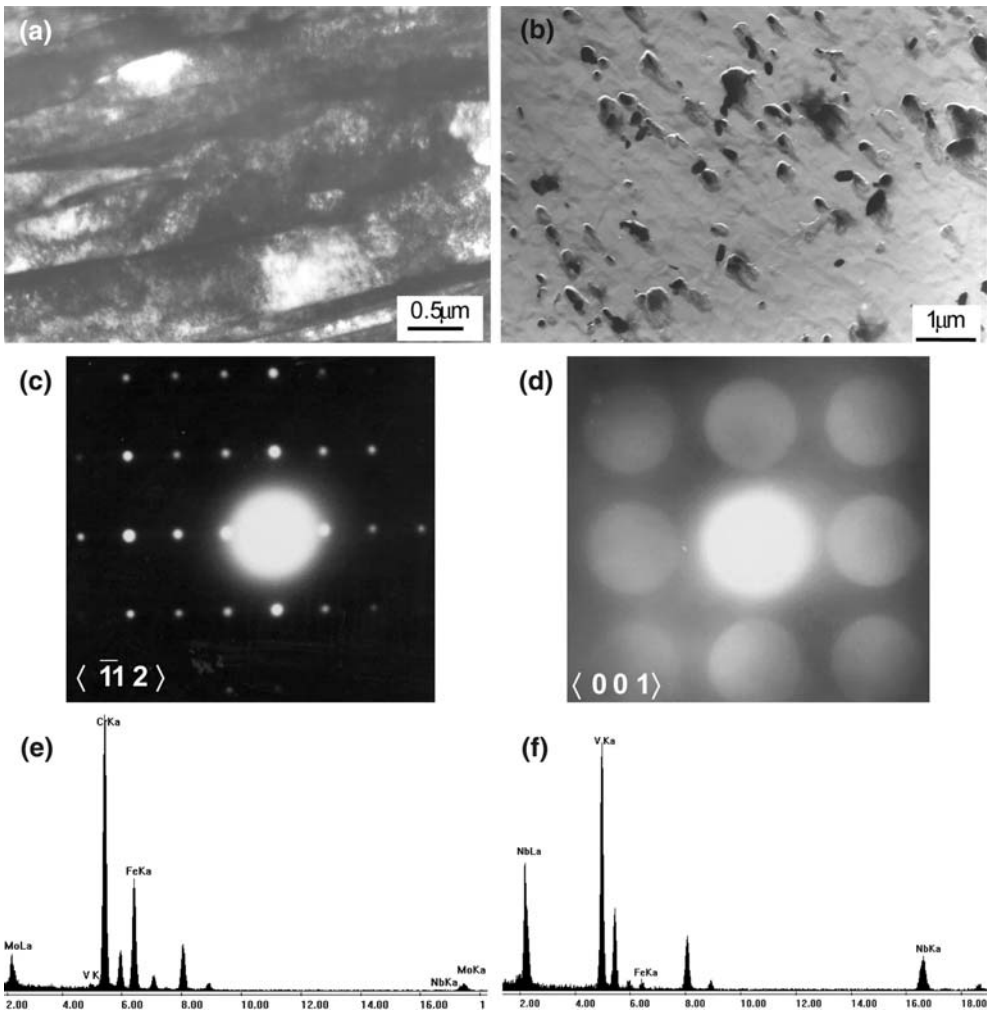

Fig. 9 Microstructure and identification of secondary phases in HAZ2 (**a**) Thin foil micrograph showing coarse laths compared to base metal and HAZ1 (**b**) Presence of coarser carbides, showing incomplete dissolution of carbide (**c**) Diffraction pattern taken from $M_{23}C_6$ along $\langle \bar{1}\ 1\ 2 \rangle$ zone axis (**d**) Microdiffraction pattern taken from a MX type of precipitate along $\langle 0\ 0\ 1 \rangle$ zone axis (**e**) EDS spectrum showing evidence for presence of $M_{23}C_6$ carbides with lower Cr/Fe ratio, and (**f**) EDS spectrum from a MX type carbide confirming V(Nb)X

dissolution of all coarse $M_{23}C_6$ carbides in this region could not have been possible. The carbides with lower Cr/Fe values could have precipitated during the cooling process.

Based on the above results, the possible reaction in the CGHAZ near the weld interface can be summarized as

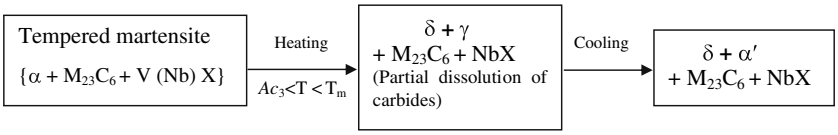

Microstructure of HAZ2

A section of HAZ away from the fusion zone was designated as HAZ2. The Prior Austenite Grain Size (PAGS) in this region was found to be 12–15 μm (Fig. 7c), which suggests that this region could be a part of FGHAZ. This

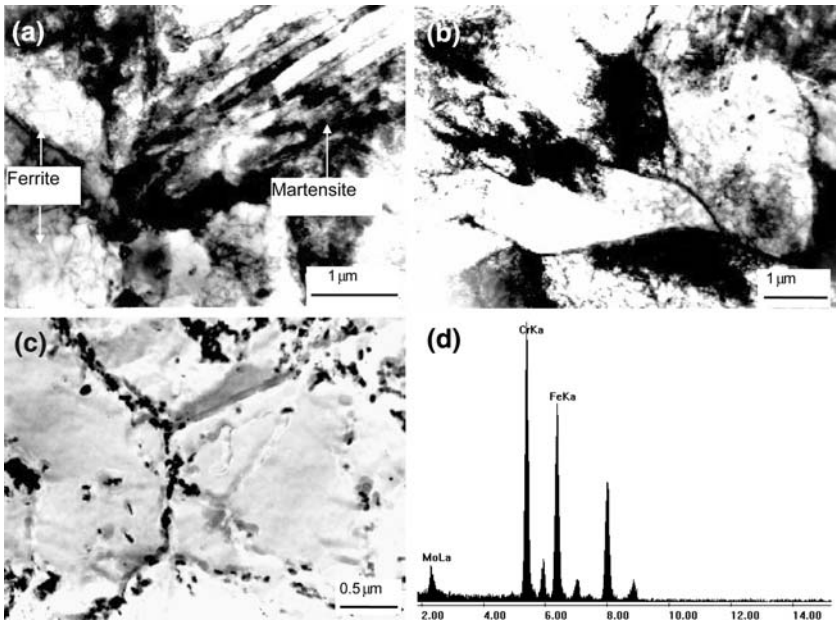

Fig. 10 Typical microstructure of Intercritical Zone (**a**) thin foil TEM micrograph showing the co-existence of ferrite and martensite (**b**) presence of ferrite (with low dislocation density) with a subgrain morphology (**c**) TEM micrograph of carbon extraction replica showing extensive carbide precipitation along martensitic lath and ferrite boundaries and within the ferrite grains, and (**d**) EDS spectrum from $M_{23}C_6$ carbide showing a low Cr/Fe ratio

region consisted of a martensitic microstructure although the average hardness was only about 300 VHN. The lower hardness could be attributed to the low carbon content in this region due to incomplete dissolution of carbides, which is also responsible for the low PAGS. This suggests that the temperature witnessed by this region would be only slightly above Ac_3. The thin-foil TEM micrograph from this region (Fig. 9a) shows the presence of lath martensite. The laths were found to be slightly coarser (0.8–1 μm) in this region as compared to base metal (0.7 μm), which suggests that the cooling rate has been low. The TEM micrograph (Fig. 9b) from the extraction replica also shows coarser lath boundary carbides of average size 0.2 μm as compared to HAZ1 where the maximum size was 0.1 μm. The number density of carbides had increased as compared to base metal, with both interlath and intralath precipitates distributed uniformly. Figure 9c and d shows the SAD pattern from two types of carbides, which were identified as $M_{23}C_6$ and MX along $\langle \bar{1}\ 1\ 2 \rangle$ and $\langle 0\ 0\ 1 \rangle$ axis respectively. The EDS spectra from the two types of carbides shown in Fig. 9e and f confirm the presence of Cr-rich $M_{23}C_6$ and V-rich MX type of carbides. Although the composition and maximum size of most of the $M_{23}C_6$ carbides were comparable to those in the base metal, additional precipitation of a large number of fine $M_{23}C_6$ (having a lower Cr/Fe ratio) and MX carbides was observed. This could be attributed to autotempering during cooling, due to low cooling rate experienced by this region.

As discussed earlier, the fine size of the prior austenite grains and high number density of carbides are in support of a low austenitization temperature experienced by this region. The possible transformation in this region can be summarized as follows:

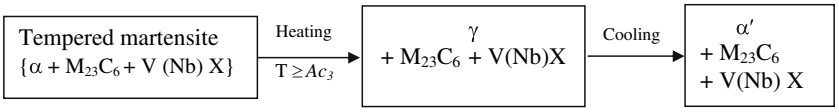

Since the maximum temperature experienced at each microscopic region depends on its distance from the heat source, it is expected that there would be a plane/zone where the maximum temperature would be between Ac_3 *and* Ac_1 corresponding to the duplex phase field. This region, termed the Intercritical region, is described below.

Intercritical region (ICHAZ)

As described previously, the microstructures in HAZ1 and HAZ2 were fully martensitic, confirming that they transformed from the austenite phase field. The inter-critical region was located by controlled removal of layers.

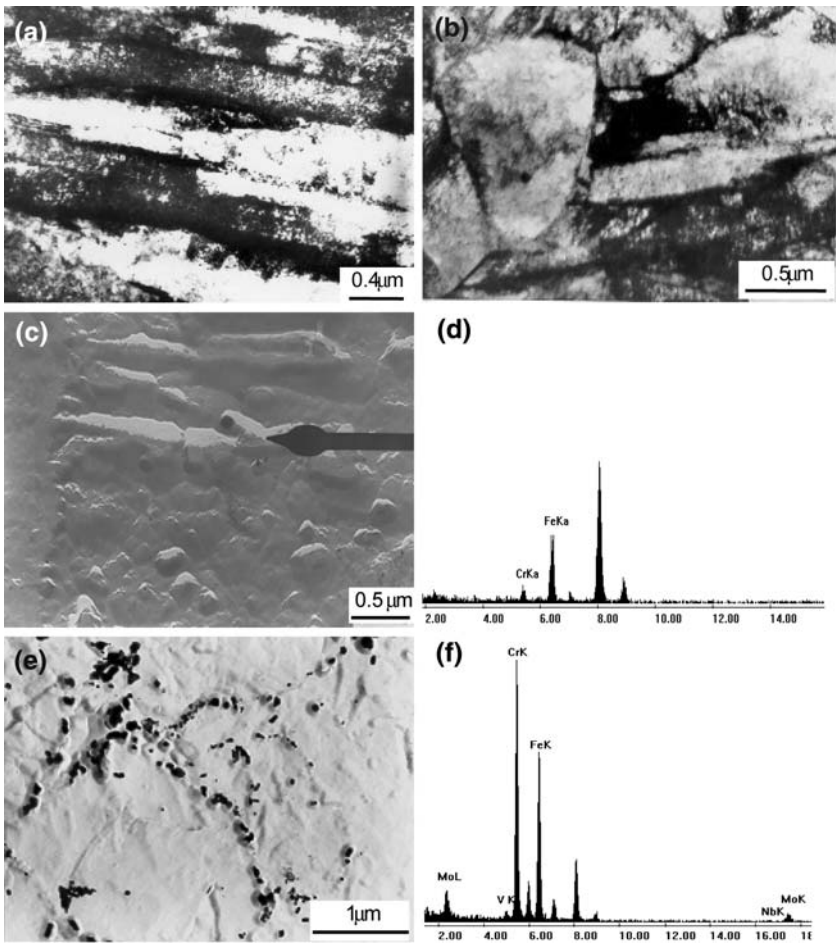

Fig. 11 Microstructural and microchemical variations within the weld region (**a**) Thin-foil TEM micrograph from region WII showing coarse lath martensite (**b**) Presence of subgrains and equiaxed ferrite in W3. (**c**) TEM micrograph of carbon extraction replica from W2, showing very fine carbides (**d**) EDS spectrum from $M_{23}C_6$ (Fe-rich) carbide present in W2 (**e**) Abundance of carbides in region W3, and (**f**) Typical EDS spectra from $M_{23}C_6$ in region W3 showing an enhancement in Cr

Figure 10a and b shows the TEM micrographs of a cross-section. The co-existence of ferrite and martensite is clearly seen, with the ferrite characterized by low dislocation density. The presence of strain-free ferrite (Fig. 10b) with morphology of a subgrain is observed. The TEM micrograph of the carbon extraction replica (Fig. 10c) shows extensive precipitation along martensitic lath and ferrite boundaries and within the ferrite grains. The lath boundary carbides could be pre existing carbides, due to low austenitization temperature. Using microchemistry as a signature of the type of carbide, a large number of very fine V and Nb carbides (<100 nm) were observed in the ferrite region. Additionally, fine $M_{23}C_6$ type carbides (Fig. 10d) with low Cr/Fe ratio (0.9–1.2) was also observed in this region. This is attributed to the fresh nucleation of $M_{23}C_6$ carbides in this temperature regime, due to maximum precipitation kinetics, since it is close to the nose temperature of the TTT diagram for this steel.

Table 4 Comparison of FWHM of ⟨1 1 1⟩ peak and relative strain with respect to base metal, for different regions of weld

Section	FWHM (Deg.)	Relative increase in microstrain w.r.t base metal (%)
Base metal	2.0	–
W1	3.5	75
W2	3.0	50
W3	2.5	25

The above observations clearly suggest that the steel in this region experienced a temperature in the duplex ($\alpha + \gamma$) phase field i.e. between Ac_1 and Ac_3. Hence, this region corresponds to the 'Intercritical' zone, where austenite and pro-eutectoid ferrite co-exist. The austenite transforms to martensite below M_s, while the ferrite remains unchanged. The low values of microhardness (~300VHN) are in agreement with the presence of small amounts of soft ferrite phase in a martensite matrix. The fine size of ferrite precluded the measurement of hardness. The presence of a soft phase embedded in a hard matrix could be responsible for the large number of failures observed in the ICHAZ due to the weak interface between them.

The reactions in the intercritical region may summarized as

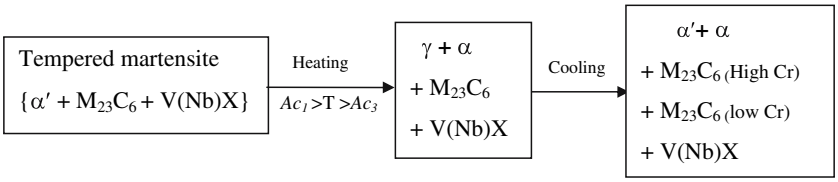

Effect of reheating on the microstructure of weld zone

The weld zone of 6 mm consisted of five layers made one over another, with the top layer alone representing the region that has undergone the L $\rightarrow$ γ $\rightarrow$ α' transformation. The regions beneath have undergone modification due to the subsequent passes laid. The microstructural modification in the weld has been studied by dividing the region into three sections namely W1, W2 and W3, parallel to fusion boundary.

It may be recalled that the solidification structure in region W1 consisted of columnar prior austenite grains with a fine martensitic structure (Fig. 5). The thin-foil TEM micrographs from regions W2 and W3 are given in Fig. 11a and b. Coarsening of laths (0.5–0.7 μm) in region W2 and presence of subgrains and equiaxed ferrite in region W3 in addition to martensitic laths is observed. Since region W3 is closest to the fusion boundary, it is expected that the effect of multiple passes would be maximum, resulting in considerable tempering in this region. This region also shows low hardness (~300VHN), which is in support of the observed microstructure. The process of welding introduces strain in a material the extent of which varies depending on the temperature cycles experienced, which will be discussed in the next section.

Relative strain measurement using XRD

The decrease in defect density, which contributed to the decrease in hardness, was studied by X-ray diffraction. Full Width at Half Maxima (FWHM) measurements were used to evaluate relative strain within the weld, using the base metal as a reference. The relative strain with respect to base metal can be expressed as

$$\%S = \left[\left(\mathrm{FWHM}_{(\mathrm{Weld})} - \mathrm{FWHM}_{(\mathrm{BaseMetal})}\right)/\mathrm{FWHM}_{(\mathrm{BaseMetal})}\right] \times 100$$

The FWHM values and % strain values thus evaluated are given in Table 4. From the table it is clear that region

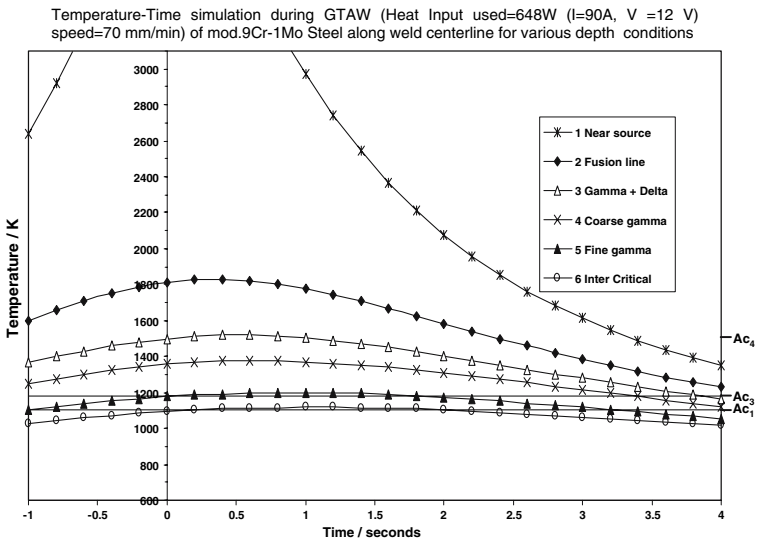

Fig. 12 Temperature profile during GTAW welding at different regions of weldment

W1 of weld has highest defect density. This is understood in terms of the large number of defects introduced during fast cooling from liquid that also results in the fine lath size, which contributes to line broadening. As described earlier, this section of the weld also showed maximum hardness. The continuous decrease in residual strain towards region W3 arises by progressive tempering due to multipass welding. This was clearly reflected in the microhardness profile.

The absence of carbides in region W1 has been discussed earlier in section 'Microstructural characterization of weld zone'. The TEM micrograph of replica obtained from region W2 is shown in Fig.11c. The presence of few fine carbides was observed which were identified as $M_{23}C_6$ type. The size of the carbides was in the range of 50–60 nm. The EDS analysis (Fig 11d) of these carbides showed that they were rich in Fe. The composition of the carbide indicates that tempering is in the initial stage. It is known that low temperature or short time of tempering in 9Cr-1Mo steel results in the formation of Fe-rich $M_{23}C_6$ [7] due to slow diffusion kinetics of chromium. In contrast, region W3 showed an abundance of carbides mostly along the grain boundaries (Fig. 11e) with sizes ranging from 50 nm to 100 nm. The carbides present were identified as $M_{23}C_6$ and found to be both iron- and chromium-rich. A typical EDS spectrum from a carbide is shown in Fig. 11f. Although chromium-rich, the Cr/Fe ratio (~1.3) was found to be lower, compared to $M_{23}C_6$ in the base metal (~2.5). This suggests that although region W3 has undergone considerable tempering, the extent of tempering is less than that in base metal. Based on the observed microstructural variations, which is an outcome of the different temperature cycles experienced by each region, an attempt has been made to predict the thermal cycles of different regions of the weldment, which is described in the next section.

Thermal cycles of different regions of weldment

In the previous section, the microstructural and microchemical modifications that take place in different regions of the weld as well as the base metal have been described. It is known that these microscopic changes are due to thermal cycles experienced, which is related to the distance of each region from the weld interface. The important parameters of the thermal cycle closely associated with phase transformations are (1) Maximum temperature (T_{max}) experienced by each region (2) Hold time at that temperature and (3) Cooling time (t_{8-5}). Using Rosenthal's steady state solutions to heat transfer equation, an attempt has been made to calculate the temperature experienced at a point in the plate when the welding torch is moving at a uniform speed. To validate the application of solution to this equation, it is assumed that an autogenous weld is made on a large plate using a point source. The temperature at a point (x, y, z) is given [29] by

$$T = T_0 + (q_0/2\pi\lambda)(1/R)\exp[-v/2a(R + x)] \quad (1)$$

where, $R = (x^2 + y^2 + z^2)^{1/2}$, q_0 = heat input = $V \times I \times \eta$, V = Voltage, I = Current, η = arc efficiency = 0.6 (for GTAW), λ = thermal conductivity, a = heat diffusivity = $\lambda/\rho c$, ρ = density (kg/m^3), c = heat capacity (J/kg K) and v = welding speed.

Temperatures were calculated for different x (distance) and z (depth) with respect to time (t), which are shown in Fig. 12, with each curve showing the heating/cooling experienced by a point at a particular depth. The curves for which maximum temperature (T_{max}) corresponds to critical temperatures have been drawn, such that each curve represents the thermal cycle experienced by a particular region of the weldment. The maximum temperature (>T_m) attained by the base metal at the fusion zone depends on the heat input. The lowest temperature of concern is the tempering temperature 1,033 K below which no transformation is possible. Generally, the different regions of the base metal that undergo modifications experience a temperature maximum between T_m and 1,033 K.

The temperatures corresponding to the different regions are as follows:

- Curve '1' represents the region very near to the heat source.
- Curve '2' stands for the region of fusion line, where $T_{max} = T_m$.
- Curve '3' represents the region, which has not liquefied but heated to $\gamma + \delta$ region.
- Curve '4' corresponds to high austenitization temperature resulting in coarse prior austenite grains.
- Curve '5' represents a temperature just above *Ac* the region of fine-grained prior austenite.
- Curve '6' depicts the ''intercritical'' region where the temperature is between Ac_3 and Ac_1. Regions far away, where the temperature is below tempering temperature, are not expected to undergo any microstructural changes.

Reactions in the different regions can be summarized as follows:

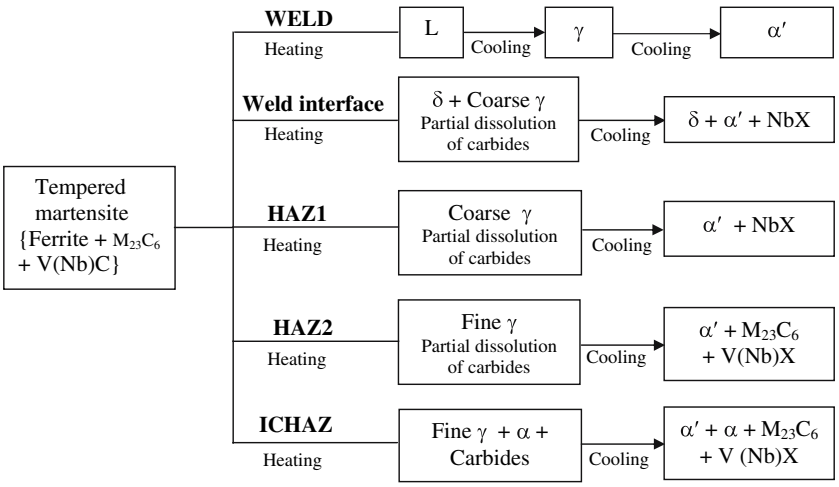

Conclusions

The microstructural and microchemical variations in different regions of a weldment of modified 9Cr-1Mo steel have been studied. Based on detailed analytical microscopy studies on different cross sections of the weldment, distinct microstructural zones have been identified. The possible thermal cycles experienced by different regions of the weld have been plotted using Rosenthal's solution to heat transfer equation and correlated with the distinct microstructural features present in each region. Finally, a comprehensive transformation sequence describing various regions of the weldment has been presented.

Acknowledgements The authors wish to acknowledge the keen interest and constant encouragement provided by Dr. V. S. Raghunathan, former Associate Director, Materials Characterisation Group and Dr. Baldev Raj, Director, Indira Gandhi Centre for Atomic Research, Kalpakkam in the pursuit of their studies on ferritic steels. The authors also thank Mr. T. Karthikeyan and Dr. S. K. Albert, scientists at Metallurgy and Materials Group, for many useful discussions.

References

1. Sikka VK (1984) In: Davis JW, Michel DJ (eds) Topical conf. on ferritic alloys for use in nuclear energy technologies. Met. Soc., AIME, Warrendale, PA, p 317
2. Klueh RL, Harries DR (2001) High-chromium ferritic and martensitic steels for nuclear applications, ASTM monograph 3. American Society for Testing and Materials, West Conshohocken, PA
3. Brinkman CR, Gieseke B, Maziasz PJ (1993) In: Liaw PK et al (eds) Microstructure and mechanical properties of aging material. TMS, Warrendale, PA, p 107
4. Cerri E, Evangelista E, Spigarelli S, Bianchi P (1998) Mater Sci Eng A245:285
5. Bhadeshia HKDH (2001) ISIJ Int 41(6):626
6. Sanderson SJ (1978) In: Pugh SF, Little EA (eds) Proceedings of international conference on ferritic steels for fast reactor steam generators. BNES, London, p 247
7. Jones WB, Hills CR, Polonis DH (1991) Metall Trans 22A:1049
8. Vitek JM, Klueh RL (1983) Metall Trans 14A:1051
9. Hald J (1996) Steel Res 67(9):369
10. Ellis FV, Viswanathan R (1998) Integrity of high temperature welds. Professional Publishing Ltd., London, UK, p 125
11. Bell K (1997) Elevated temperature midlife weldment cracking, Report 597/1997. The Welding Institute, Abinington, UK
12. Laha K, Chandravathi KS, Bhanu Sankara Rao K, Mannan SL, Sastry DH (2001) Metall Mater Trans 32A:115
13. Albert SK, Matzui M, Watanabe T, Hongo H, Kubo K, Tabuchi M, (2002) ISIJ Int 42(12):1497
14. Albert SK, Matsui M, Hongo H, Watanabe T, Kubo K, Tabuchi M (2004) Int J Pres Ves Pip 81:221
15. Raj B, Choudhary BK, Singh Raman RK (2004). Int J Pres Ves Pip 81:521
16. Chandravathi KS, Laha K, Bhanu Sankara Rao K, Mannan SL (2001) Mater Sci Tech 17:559
17. Pesicka J, Kuzel R, Dronhofer A, Eggler G (2003) Acta Mat 51:4847
18. Foldyna V, Jakobava A, Vodarek V, Kubon Z (1994) In: Coutsouradis D et al (eds) Proceedings of 5th conference on materials for advanced power engineering, October 1994. Liege, Belgium, p 453
19. Spigarelli S, Cerri E, Bianchi P, Evangelista E (1999) Mater Sci Tech 15:1433
20. Patriarca P, Harkness SD, Duke JM, Cooper LR (1976) Nucl Tech 28:516
21. Iseda A, Sawaragi Y, Kato S, Masuyama F (1992) In: Proceedings of 5th international conference on creep materials. ASM Int., Materials Park, OH, p 389
22. Sireesha M, Albert SK, Sundaresan S (2001) Sci Technol Weld Joi 6(4):247
23. Brozda J, Zeman M (2003) Eng Fail Anal 10:569
24. Allen DJ, Brett SJ (1999) In: Proceedings of international symposium on case histories on integrity and failures in industry, held in Milan, Italy, 1999. Engineering Materials Advisory Services Ltd, London, UK, p 133

25. Brett SJ, Allen DJ, Pacey J (1999) In: Proceedings of international symposium on case histories on integrity and failures in industry, held in Milan, Italy, 1999. Engineering Materials Advisory Services Ltd, London, UK, p 873
26. Sanderson SJ (1983) In: Khare AK (ed) Proceedings of conference on ferritic steels for high-temperature applications. Warrendale, PA, 1981. Asm Metals Park, p 85
27. Vijayalakshmi M, Saroja S, Thomas Paul V, Mythili R, Raghunathan VS (1999) Metall Trans 30A:161
28. Kishore R, Singh RN, Sinha TK, Kashyap BP (1992) J Nucl Mater 195:198
29. Grong O (1997) In: Metallurgical modelling of welding, 2nd edn. The Institute Of Materials, London, UK, p 28